CrossMark

J. Fluid Mech. (2016), *vol.* 803, *pp.* 175–199. © Cambridge University Press 2016
doi:10.1017/jfm.2016.514

Transition in the asymptotic suction boundary layer over a heated plate

Stefan Zammert[1,2,†], Nicolas Fischer[3] and Bruno Eckhardt[1,4]

[1]Fachbereich Physik, Philipps-Universität Marburg, D-35032 Marburg, Germany

[2]Laboratory for Aero and Hydrodynamics, Delft University of Technology, 2628 CD Delft, The Netherlands

[3]Fakultät Verkehrswissenschaften "Friedrich List", Technische Universität Dresden, D-01062 Dresden, Germany

[4]J.M. Burgerscentrum, Delft University of Technology, 2628 CD Delft, The Netherlands

(Received 23 May 2016; revised 23 May 2016; accepted 1 August 2016; first published online 19 August 2016)

The asymptotic suction boundary layer (ASBL) is a parallel shear flow that becomes turbulent in a bypass transition in parameter regions where the laminar profile is stable. We here add a temperature gradient perpendicular to the plate and explore the interaction between convection and shear in determining the transition. We find that the laminar state becomes unstable in a subcritical bifurcation and that the critical Rayleigh number and wavenumber depend strongly on the Prandtl number. We also track several secondary bifurcations and identify states that are localized in two directions, showing different symmetries. In the subcritical regime, transient turbulent states which are connected to exact coherent states and follow the same transition scenario as found in linearly stable shear flows are identified and analysed. The study extends the bypass transition scenario from shear flows to thermal boundary layers and highlights the intricate interactions between thermal and shear forces.

Key words: boundary layers, convection, nonlinear dynamical systems

1. Introduction

Thermal transport in shear flows is a fundamental problem in fluid mechanics that arises in many engineering and geophysical situations. It combines phenomena in fluid layers without external shear (the Rayleigh–Bénard (RB) flow (Chandrasekhar 1961)) and in shear flows without heating (Grossmann 2000; Schmid & Henningson 2001). The onset of convection in the RB setting has been studied in considerable detail in various geometries (Busse 1978). The properties of shear flows are less well understood because of the difficulties presented by the manner in which they become turbulent (Grossmann 2000; Schmid & Henningson 2001). In contrast to RB flows, turbulence in shear flows is often observed when the laminar profile is still linearly stable, so that the transition requires finite-amplitude perturbations that reach states that arise in subcritical bifurcations (Eckhardt *et al.* 2007). The advective nature and the spatial development in open boundary layers add to the complexity.

† Email address for correspondence: Stefan.Zammert@gmail.com

https://doi.org/10.1017/jfm.2016.514 Published online by Cambridge University Press

The interaction between shear and convection has been studied in boundary layers (Sparrow & Cess 1961; Merkin 1972), where it affects the functional form of the profile (Marati *et al.* 2006). The dynamics of plumes and other structures has been investigated in the context of RB flows (Ahlers, Grossmann & Lohse 2009; Chillà & Schumacher 2012) because of their contribution to the heat transport (Zocchi, Moses & Libchaber 1990; Parodi *et al.* 2004; Zhou, Sun & Xia 2007; Zhou & Xia 2010). The presence of instabilities is connected with a transition that also marks the entry into the ultimate regime (Grossmann & Lohse 2000*a*, 2002). Experiments by Du Puits *et al.* (2013) show that the flow in the transition region can be spatially localized and transient, very much as in the case of bypass transition in shear flows. A quantitative study focusing on the hydrodynamic instabilities in heated boundary layers does not seem to have been published.

The manner in which shear and buoyancy interact to shape the transition has been studied by Clever & Busse (1992) for the case of RB with a linear shear. They identified the onset of modulated rolls and the transition to a subcritical regime when the shear was strong and the temperature gradient weak. Ultimately, this state could be traced to an exact coherent structure (ECS) in plane Couette flow that is related to the transition in the pure shear flow without a temperature gradient. The ECS reached via heating coincides with the one obtained by adding rotation as a destabilizing force (Nagata 1990). Using these and related embeddings, as well as some other techniques (Dijkstra *et al.* 2014), numerous exact coherent structures have been identified in plane Couette flow (Nagata 1990; Schmiegel 1999; Gibson, Halcrow & Cvitanović 2009), in pipe flow (Faisst & Eckhardt 2003; Hof *et al.* 2004; Wedin & Kerswell 2004; Pringle & Kerswell 2007; Duguet, Pringle & Kerswell 2008; Eckhardt *et al.* 2008), in plane Poiseuille flow (Waleffe 2001; Nagata & Deguchi 2013; Gibson & Brand 2014; Zammert & Eckhardt 2014*a*,*b*) and even in boundary layers (Duguet *et al.* 2012). For these flows the observed transient subcritical turbulence could be explained by ECS which create a chaotic saddle in a series of bifurcations (Kreilos & Eckhardt 2012; Avila *et al.* 2013; Zammert & Eckhardt 2015). Further studies have shown that ECS are linked dynamically (Halcrow *et al.* 2009) and embedded in the turbulent dynamics (Kawahara & Kida 2001).

The asymptotic suction boundary layer (ASBL) (Schlichting & Gersten 1997) is a boundary layer that is of interest on its own because of its relation to flow control since suction stabilizes the boundary layer. It is also of theoretical interest since the flow is parallel and can hence be studied using the tools developed for parallel shear flows. Experimental realizations of both the pure shear flow (Fransson & Alfredsson 2003) and the heated version (Moffat & Kays 1968) are available. Taking the cross-flow as a parameter, the ECS from plane Couette flow could be traced to ASBL and a transition in the dynamics could be identified (Kreilos *et al.* 2013; Kreilos, Gibson & Schneider 2016). Further ECS for ASBL, in the form of travelling waves and periodic orbits, have been identified and studied (Khapko *et al.* 2013, 2014; Deguchi & Hall 2014). We here expand the analysis of the ASBL to include heating of the bottom plate, so as to form a thermal asymptotic suction boundary layer (TASBL). The study of such a parallel TASBL contributes to our understanding of the turbulence transition and the dynamics of coherent structures in thermal boundary layers.

The further outline of this paper is as follows: in § 2, we introduce the system and its laminar solution. The stability of the base flow as a function of Rayleigh number, Reynolds number and Prandtl number and the two-dimensional secondary solutions bifurcating from the laminar state are discussed in § 3. In § 4 examples of the cascade of bifurcations that lead to a chaotic saddle and subcritical chaos in the system are

https://doi.org/10.1017/jfm.2016.514 Published online by Cambridge University Press

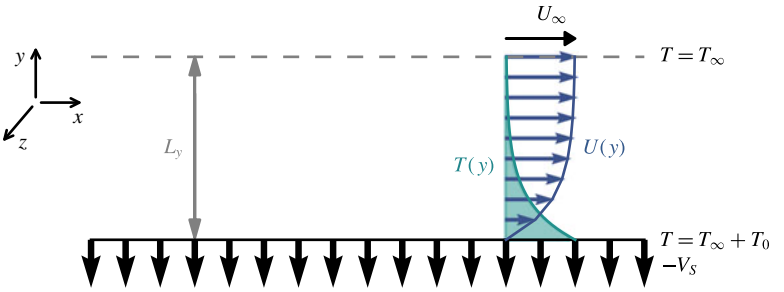


FIGURE 1. (Colour online) Sketch of the ASBL over a heated plate. Far above the plate the flow moves with speed U_∞ in the streamwise direction. The temperature difference between the plate and the fluid far above the plate is T_0. In the numerical simulation the domain is closed from above with a plate at a height L_y, indicated by a grey line.

studied. Finally, in § 5 three-dimensional secondary bifurcations are analysed, with a particular emphasis on exact solutions that are localized in both directions parallel to the plate. We end with an outlook in § 6.

2. Description of the system and its laminar state

The asymptotic suction boundary layer is the flow over a plate through which fluid is sucked homogeneously with a speed $-V_S$. Far above the plate, the parallel velocity component of the flow has a speed U_∞. For TASBL there is a temperature difference T_0 between the plate and the fluid far above the plate. The flow geometry of TASBL is sketched in figure 1.

The flow is governed by the Overbeck–Boussinesq equations (Landau & Lifschitz 1959)

$$\partial_t \boldsymbol{u} + (\boldsymbol{u}\cdot\boldsymbol{\nabla})\boldsymbol{u} = -\boldsymbol{\nabla} p + \nu\Delta\boldsymbol{u} + \beta g\theta \boldsymbol{e}_y, \tag{2.1}$$

$$\partial_t \theta + (\boldsymbol{u}\cdot\boldsymbol{\nabla})\theta = \kappa\Delta\theta, \tag{2.2}$$

$$\Delta\boldsymbol{u} = 0, \tag{2.3}$$

where ν is the kinematic viscosity, κ the thermal diffusivity, β the thermal expansion coefficient and g the gravitational acceleration, pointing in the y-direction perpendicular to the plate. The boundary conditions of the system are

$$u(y=0) = 0 \quad \text{and} \quad u(y=\infty) = U_\infty, \tag{2.4a,b}$$

$$v(y=0) = v(y=\infty) = -V_S, \tag{2.5}$$

$$\theta(y=0) = T_0 \quad \text{and} \quad \theta(y=\infty) = 0. \tag{2.6a,b}$$

The stationary laminar profile for the velocity is given by

$$\boldsymbol{U}(x, y, z) = (U(y), -V_s, 0) \quad \text{with } U(y) = U_\infty(1 - \mathrm{e}^{-V_s y/\nu}) \tag{2.7}$$

and the deviation of the temperature from the background temperature T_∞ is given by

$$T(x, y, z) = T_0 \cdot \mathrm{e}^{-V_s y/\kappa}. \tag{2.8}$$

https://doi.org/10.1017/jfm.2016.514 Published online by Cambridge University Press

A characteristic length scale of the system is the displacement thickness (Schlichting & Gersten 1997)

$$\delta = \int_0^\infty \left(1 - \frac{U(y)}{U_\infty}\right) \mathrm{d}y = \frac{\nu}{V_S}. \tag{2.9}$$

The dimensionless numbers characterizing the system are the Reynolds, Prandtl and Rayleigh number, given by

$$Re = \frac{U_\infty \delta}{\nu} = \frac{U_\infty}{V_s}, \quad Pr = \frac{\nu}{\kappa}, \quad Ra = \frac{\beta g \delta^3 T_0}{\kappa \nu}. \tag{2.10a–c}$$

The equations can be made dimensionless by measuring lengths in units of δ, time in units of δ^2/κ (corresponding to measuring velocities in units of κ/δ) and temperature in units of T_0/Ra:

$$\partial_t \boldsymbol{u} + (\boldsymbol{u}\cdot\boldsymbol{\nabla})\boldsymbol{u} = -\boldsymbol{\nabla} p + Pr\,\Delta \boldsymbol{u} + Pr\,Ra\,\theta \boldsymbol{e}_y, \tag{2.11}$$

$$\partial_t \theta + (\boldsymbol{u}\cdot\boldsymbol{\nabla})\theta = \Delta\theta, \tag{2.12}$$

$$\boldsymbol{\nabla}\cdot\boldsymbol{u} = 0. \tag{2.13}$$

The non-dimensionalized laminar profiles become

$$\boldsymbol{U}(x, y, z) = (U(y), -Pr, 0), \quad U(y) = Pr\,Re(1 - \mathrm{e}^{-y}), \tag{2.14a,b}$$

$$T(x, y, z) = Ra\,\mathrm{e}^{-Pr\,y}. \tag{2.15}$$

The thickness δ_θ of the thermal boundary layer is then inversely proportional to the Prandtl number,

$$\delta_\theta = \frac{\delta}{Pr}. \tag{2.16}$$

Thus, the Prandtl number can also be interpreted as the ratio between the thicknesses of the velocity boundary layer δ and the thermal boundary layer δ_θ. For values of Pr smaller than unity (e.g. air and liquid metals) the thermal boundary layer is thicker than the velocity boundary layer. For $Pr = 1$ both have the same thickness, while for $Pr > 1$ (e.g. water and oils) the thermal boundary layer is the thinner one.

The velocity and temperature fields are decomposed into a base flow and fluctuations,

$$\theta = T + \theta', \tag{2.17}$$

$$\boldsymbol{u} = \boldsymbol{U} + \boldsymbol{u}'. \tag{2.18}$$

Unless stated explicitly, only the fluctuations θ' and $\boldsymbol{u}'$ are visualized or used in bifurcation diagrams.

In the numerical simulations the wall-normal direction has to be truncated at some distance L_y. To this end, the system is closed with a permeable plate with asymptotic temperature and velocity components, and no-slip boundary conditions for the deviations. The modified base profiles become

$$U^*(y) = Re\,Pr \frac{1 - \mathrm{e}^{-y}}{1 - \mathrm{e}^{-L_y}} \tag{2.19}$$

and

$$T^*(y) = \frac{Ra}{1 - \mathrm{e}^{-Pr\,L_y}} (\mathrm{e}^{-Pr\,y} - \mathrm{e}^{-Pr\,L_y}). \tag{2.20}$$

https://doi.org/10.1017/jfm.2016.514 Published online by Cambridge University Press

In all simulations a value of L_y equal to or larger than 20 is used. In all simulations it was carefully checked that this value was sufficiently big so that the differences between the asymptotic profiles $U(y)$ and $T(y)$ and the finite profiles $U^*(y)$ and $T^*(y)$ remained small.

A quantity of particular interest in the study of thermal systems is the heat flux, which has a convective and a conductive contribution. For the base flow, the convective heat flux is given by

$$\phi_{conv}(y) = \langle v \cdot T \rangle_{x,z} = -Pr\,Ra\,\mathrm{e}^{-Pr\,y}. \tag{2.21}$$

For the conductive heat flux we find

$$\phi_{cond}(y) = -\partial_y \langle T \rangle_{x,z} = Pr\,Ra\,\mathrm{e}^{-Pr\,y}. \tag{2.22}$$

Thus, in contrast to Rayleigh–Bénard convection, the conductive heat flux of the base flow depends on the wall-normal coordinate y. Moreover, the conductive and convective contributions cancel, and the total heat transfer of the laminar state vanishes. This is no longer the case for the turbulent states. As a dimensionless measure for the heat flux we introduce the Nusselt number Nu, the ratio of the total heat flux to the conductive heat flux of the base flow at the wall $\phi_{cond}(0)$,

$$Nu = \frac{\phi_{conv} + \phi_{cond}}{\phi_{cond}(0)} \tag{2.23}$$

$$= \frac{\langle (-Pr + v)(\theta' + T) \rangle_{x,z} - \partial_y \langle \theta' + T \rangle_{x,z}}{Pr\,Ra}. \tag{2.24}$$

In order to eliminate the dependence on the wall-normal coordinate, we integrate over y and introduce

$$\tilde{Nu} = \int_0^\infty Nu(y)\,\mathrm{d}y, \tag{2.25}$$

the volume-integrated heat flux.

3. Stability analysis and secondary solutions

In this section the stability of the laminar state is analysed and the bifurcating secondary solutions are discussed. The linear stability of the flow is determined by solving the Orr–Sommerfeld equations for the flow. The derivation of the equations follows the usual steps and is described in § 3.1. Direct numerical simulation is used to identify exact solutions of the equations. For the simulations we used the Channelflow-code (Gibson 2012) (www.channelflow.org), which we enhanced to handle a temperature field. Details of the modification are given in appendix A.

Following the derivation of the stability equations, we will first analyse the case $Ra = 0$ in § 3.2. Afterwards, we will present the result for the case $Re = 0$ in § 3.3. Finally, the combined effect of temperature and shear is discussed in § 3.4.

3.1. *Orr–Sommerfeld stability equations*

Starting point for the stability analysis are the Navier–Stokes equations (2.11)–(2.13). The full flow field $\boldsymbol{u}$ can be expressed as a sum of a base flow contribution $\boldsymbol{U}$ and a perturbation $\boldsymbol{u}'$. The temperature and pressure fields can be decomposed similarly.

https://doi.org/10.1017/jfm.2016.514 Published online by Cambridge University Press

Inserting this ansatz in the equations and neglecting the nonlinear terms in the perturbations we obtain:

$$\frac{1}{Pr}[\partial_t \boldsymbol{u}' + (\boldsymbol{u}' \cdot \nabla)\boldsymbol{U} + (\boldsymbol{U} \cdot \nabla)\boldsymbol{u}'] = -\nabla p + \Delta \boldsymbol{u}' + Ra(T + \theta')\boldsymbol{e}_y, \tag{3.1}$$

$$\partial_t \theta' + (\boldsymbol{u}' \cdot \nabla)T + \boldsymbol{U} \cdot \nabla \theta' = \Delta \theta'. \tag{3.2}$$

Form this set of equations the pressure can be removed by writing the solenoidal perturbation velocity field $\boldsymbol{u}'$ in terms of two scalar fields $\Phi(\boldsymbol{x})$ and $\Psi(\boldsymbol{x})$.

$$\boldsymbol{u}' = \nabla \times \Psi \boldsymbol{e}_y + \nabla \times (\nabla \times \Phi \boldsymbol{e}_y). \tag{3.3}$$

For the resulting three scalar fields Φ, Ψ and θ' we take Fourier series in spanwise and streamwise directions and an exponential dependence in time,

$$\Phi(\boldsymbol{x}, t) = \sum_{k_x, k_z, \sigma} \Phi_{k_x, k_z, \sigma}(y) \exp(\mathrm{i}(k_x x + k_z z) + \sigma t), \tag{3.4}$$

$$\Psi(\boldsymbol{x}, t) = \sum_{k_x, k_z, \sigma} \Psi_{k_x, k_z, \sigma}(y) \exp(\mathrm{i}(k_x x + k_z z) + \sigma t), \tag{3.5}$$

$$\theta'(\boldsymbol{x}, t) = \sum_{k_x, k_z, \sigma} \Theta_{k_x, k_z, \sigma}(y) \exp(\mathrm{i}(k_x x + k_z z) + \sigma t). \tag{3.6}$$

Using this representation of the fields, we obtain the stability equations

$$\left(\frac{\sigma}{Pr} + \frac{\mathrm{i}k_x U}{Pr} - D_y - (D_y^2 - k^2)\right)\Psi(y) + \frac{\mathrm{i}k_z U'}{Pr}\Phi(y) = 0, \tag{3.7}$$

$$\left[\left(\frac{\sigma}{Pr} + \frac{\mathrm{i}k_x U}{Pr} - D_y\right)(D_y^2 - k^2) - \frac{\mathrm{i}k_x U''}{Pr} - (D_y^2 - k^2)^2\right]\Phi(y) + Ra\Theta(y) = 0, \tag{3.8}$$

$$(\sigma + \mathrm{i}k_x U - Pr\, D_y - (D_y^2 - k^2))\Theta(y) + k^2 T' \Phi(y) = 0. \tag{3.9}$$

In this set of equations D_y denotes the derivative with respect to the wall-normal coordinate, $U(y) = Re\, Pr(1 - \mathrm{e}^{-y})$ is the streamwise component of the laminar velocity field and $T(y) = \mathrm{e}^{-Pr\, y}$ is the laminar temperature profile. k_x and k_z are the streamwise and spanwise wavenumbers, and $k = \sqrt{k_x^2 + k_z^2}$ is the wavenumber in the direction of propagation. The set of equations (3.7)–(3.9) is solved using a Chebychev spectral method (Trefethen 2000), where the Chebychev polynomials are mapped from an interval $[-1, 1]$ to an interval $[0, L_y]$ with a sufficiently large truncation length L_y.

3.2. *Stability analysis for* $Ra = 0$

For $Ra = 0$ the system reduces to isothermal ASBL. Hocking (1975) showed that the laminar profile of isothermal ASBL has a linear instability at $Re \approx 54\,370$ for a critical streamwise wavenumber $k_c = 0.1555$. The fact that ASBL becomes unstable at such a high Reynolds number compared to the Blasius boundary layer which becomes unstable at $Re_{c,BL} = 519.4$ (Schmid & Henningson 2001) shows the strongly stabilizing effect of the suction. Milinazzo & Saffman (1985) tracked the travelling wave solutions which bifurcate from the laminar profile and found that they extend down to Reynolds numbers of around 3000. To obtain the stability curve the stability equations are solved with up to 500 Chebychev polynomials and a truncation length

https://doi.org/10.1017/jfm.2016.514 Published online by Cambridge University Press

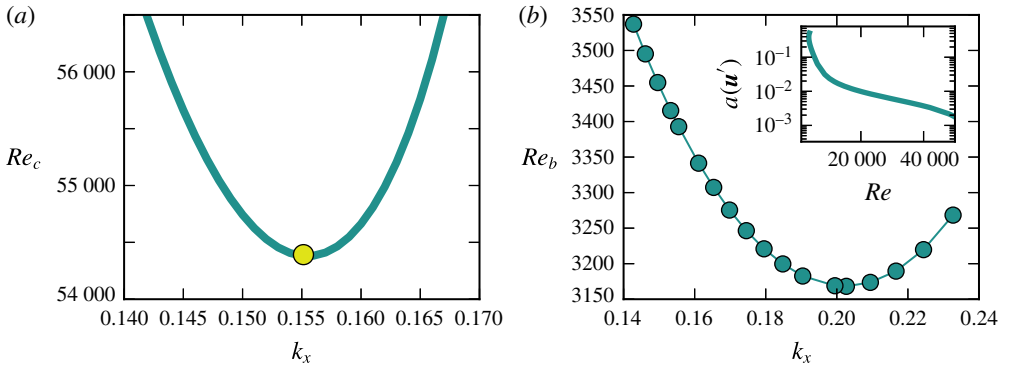


FIGURE 2. (Colour online) The stability boundary of the laminar state of isothermal ASBL ($Ra = 0$) is shown in (*a*). The critical Reynolds number $Re_c = 54\,379$ is marked by a circle. (*b*) Shows the Reynolds number Re_b of the subcritical bifurcation point for the TS-wave versus streamwise wavenumber k_x. The inset shows a bifurcation diagram of the TS-wave for $k_x = k_c$ which uses the amplitude of the flow field $a(\boldsymbol{u}')$ on the vertical axis.

of 40 in y-direction. Using a bisection, the critical value for Re is reproduced with a relative error of order 10^{-2}. Squires theorem (Gage & Reid 1968; Schmid & Henningson 2001) ensures that a two-dimensional streamwise mode is the first to become unstable so that we can restrict the Orr–Sommerfeld analysis to spanwise invariant modes ($k_z = 0$). The critical Reynolds numbers as a function of streamwise wavenumber agree with the results of Hocking (1975) and the more recent ones of Fransson & Alfredsson (2003); they are shown in figure 2(*a*). The critical Reynolds number found here is 54 379, which is achieved for a streamwise wavenumber 0.1555. Wedin, Cherubini & Bottaro (2015) showed recently that the instability of the flow moves to lower Reynolds numbers if the plate's permeability is not neglected.

The Tollmien–Schlichting-like travelling wave solution which bifurcates subcritically from the laminar flow has been traced in Re for various values of the streamwise wavenumber. A bifurcation diagram of the waves is included in figure 2(*b*) in an inset. For the ordinate of the diagram we use the amplitude,

$$a(\boldsymbol{u}') = \sqrt{\left(\frac{1}{L_x L_z}\int_{L_x}\int_{L_y}\int_{L_z} \boldsymbol{u}'^2 \,\mathrm{d}x\,\mathrm{d}y\,\mathrm{d}z\right)}, \tag{3.10}$$

of the flow field, where L_x and L_z are the streamwise and spanwise wavelengths of the computational domain. The plot shows that close to the turning point the amplitude of the flow field increases dramatically. The dependence of the positions of the turning point on the wavenumber is given in figure 2(*b*). The minimal Reynolds number of the turning point is 3168, which is achieved for $k_x = 0.203$. These results show that as in the case of plane Poiseuille flow the two-dimensional waves connected to the instability of the base flow appear at Reynolds numbers much higher than the observed onset of subcritical turbulence, which was found to be at $Re \approx 270$ for ASBL (Khapko *et al.* 2016).

Visualizations of the bifurcating two-dimensional solutions are given in figure 3 for different Reynolds numbers. Because the flow has no discrete symmetry with respect to the wall-normal direction y, the clockwise and counter-clockwise rolls behave

https://doi.org/10.1017/jfm.2016.514 Published online by Cambridge University Press

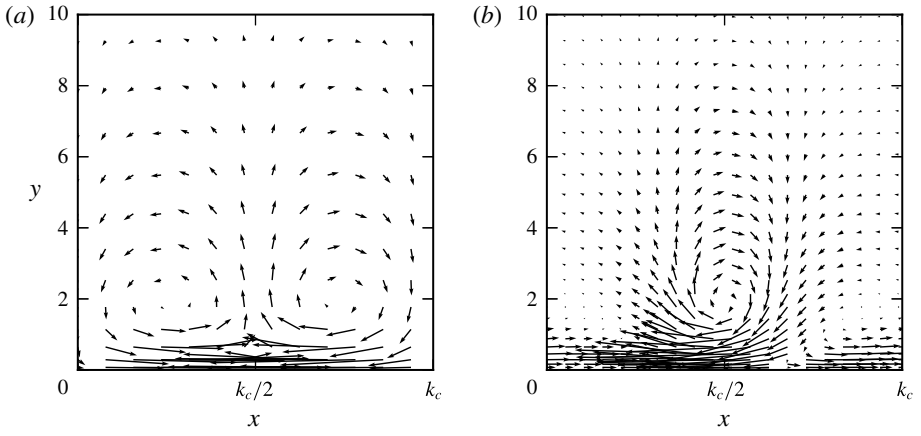


FIGURE 3. Visualizations of the TS-wave bifurcating from the base flow for $Re = 50\,000$ (a) and $Re = 8475$ (b). In both cases the streamwise wavenumber is 0.1555. The direction of the flow is from left to right.

differently with Re. Close to the bifurcation point at $Re = 50\,000$ (figure 3a) the rolls are almost symmetric. When Re is decreased the counter-clockwise roll becomes strongly deformed while the clockwise roll maintains its shape and becomes narrower only (figure 3b).

3.3. *Stability analysis for* $Re = 0$ *and* $Ra \neq 0$

We now turn to the stability of the thermal boundary layer for the case $Re = 0$. The corresponding Orr–Sommerfeld equations (3.7)–(3.9) are solved using up to 600 Chebychev polynomials and truncation lengths L_y up to 250 (for small Prandtl numbers). In figure 4 the calculated stability curves for various Prandtl numbers, including the cases $Pr = 0.7$ (air) and $Pr = 6$ (water), are shown. The results show a strong dependence on the Prandtl number and therefore on the relative size of the thermal to the viscous boundary layer that is in contrast to the standard Rayleigh–Bénard convection. For the case $Pr = 1$ a critical Rayleigh number of 19.4705 and a critical wavenumber of 0.438 are obtained. For lower values of Pr the critical wavenumber and Rayleigh number move to lower values, while they move to higher ones if larger values of Pr are considered.

The critical Rayleigh and wavenumber are shown in figure 5(a,b) in dependence on the Prandtl number. The graphs show that the dependence of the critical wavenumber on Pr is approximately linear. The Pr-dependence of the critical Rayleigh number seems to follow a power law, with an exponent near two for $Pr < 1$ and near three for $Pr > 1$.

An explanation for the Pr-dependence of the critical Rayleigh number may be obtained from a discussion of the relevant scales, similar to the one given by Grossmann & Lohse (2000b) for normal Rayleigh–Bénard convection. The definition of Ra uses the length scale of the velocity boundary layer δ and the full temperature difference. For large values of Pr the thickness of the temperature boundary layer δ_θ is much smaller than the one of the velocities. Therefore, the length scale relevant for the forces driving convection is δ_θ. A Rayleigh number based on δ_θ can be obtained by multiplication of Ra with $1/Pr^3$ because $Ra \propto \delta^3$ and $\delta/\delta_\theta = Pr$. By the same

https://doi.org/10.1017/jfm.2016.514 Published online by Cambridge University Press

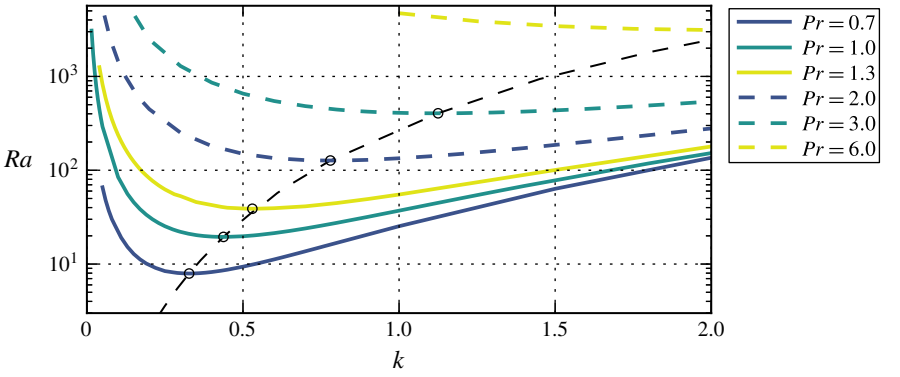


FIGURE 4. (Colour online) Stability boundary for $Re = 0$ and different values of the Prandtl number. For each Prandtl number the lowest critical Rayleigh number is marked by a black circle.

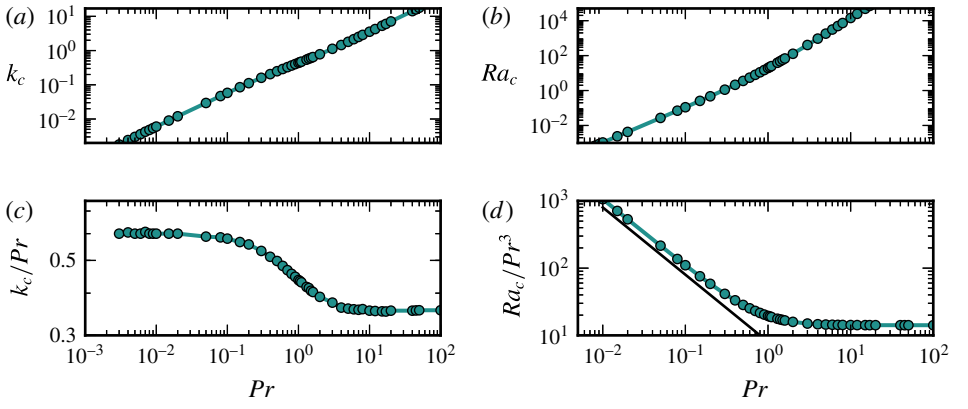


FIGURE 5. (Colour online) Prandtl number dependence of critical wavenumber and critical Rayleigh number as a function of Prandtl number are shown in (*a*,*b*), respectively. (*c*,*d*) Show the results after a change of the length scale to the thermal boundary layer thickness $\delta_\theta = \delta/Pr$. The thin black line in (*d*) indicates a Pr^{-1} scaling.

argument, the wavenumber based on δ_θ is obtained from the one based on δ by dividing by Pr. The results of this change in length scale are shown in figure 5(*c*,*d*). For the wavenumber as well as for Ra the change of the length scale leads to critical values that for large values of Pr become independent of the Prandtl number. The critical wavenumber $k_{\theta,c}$ and Rayleigh number Ra_θ based on the thickness of the temperature boundary layer that are asymptotically reached for large Prandtl numbers are 0.363 and 14.3, respectively.

For the case $Pr < 1$, two modifications have to be taken into account. The observation that the rescaled critical wavenumber reaches a plateau value for small values of Pr (see figure 5*c*), suggest that the thickness of the thermal boundary layer determines the instability also for this parameter regime. However, since the viscous boundary layer is smaller than the thermal boundary layer, the temperature drops only by a fraction $(\delta/\delta_\theta)T_0 = Pr\,T_0$, and it is this smaller range that should be taken for the temperature difference in the definition of the Rayleigh number. Accordingly,

https://doi.org/10.1017/jfm.2016.514 Published online by Cambridge University Press

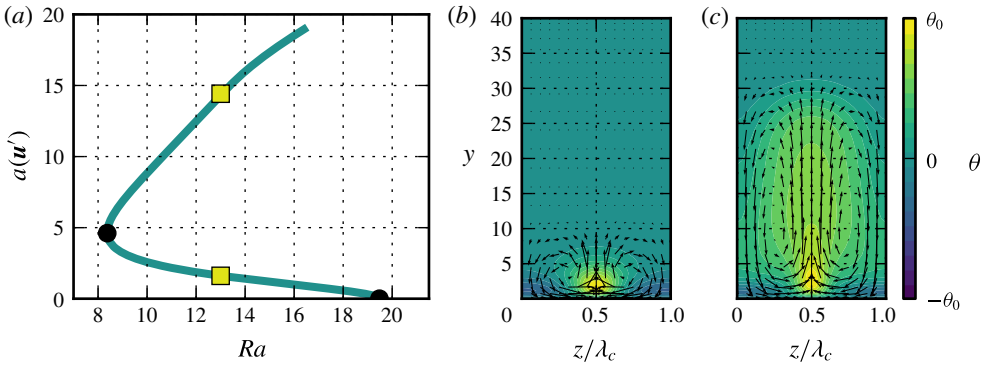


FIGURE 6. (Colour online) (*a*) Shows the bifurcation diagram of the secondary solution with $k = k_c = 0.4305$. On the y-axis the amplitude $a(\boldsymbol{u}')$ of the solution is used. (*b*,*c*) Show visualizations of the flow and temperature fields for the lower and the upper branches of R_1. The positions of the visualization are marked in (*a*) using yellow squares. The velocity field is visualized by the arrows. The temperature field is represented by the colours. For the lower branch $\theta_0 = 0.19\,Ra$ and for the upper branch $\theta_0 = 0.32\,Ra$.

there is a factor of Pr from the temperature difference, and a factor Pr^{-3} from the scaling of the height, resulting in a scaling of Pr^2 for the critical Rayleigh number, or Pr^{-1} in the scaling used in figure 5(*d*).

By using the Newton method (Viswanath 2007) included in the channelflow package, it is possible to identify the exact solutions bifurcating at the linear instability and to continue them in Rayleigh number. The used resolution is $N_x \times N_y \times N_z = 4 \times 49 \times 32$. Four modes in the x-direction are sufficient because the structures are two-dimensional and do not vary in x-direction. In the wall-normal direction a truncation length L_y is chosen which is large enough so that there is no noticeable influence on the structures by the wall. For lower branch states $L_y = 40$ is sufficient, while for upper branch states values up to $L_y = 110$ with a resolution $N_y = 129$ are necessary.

The bifurcating ECS identified by the Newton method is an equilibrium solution which we refer to as roll state R_1 in the following. A bifurcation diagram of the ECS for the critical wavenumber k_c and $Pr = 1$ is given in figure 6(*a*). The diagram shows that in contrast to the case of Rayleigh–Bénard flow the bifurcation is subcritical. For the critical wavenumber $k_c = 0.4304$ used for the bifurcation diagram, the turning point of the solutions lies at $Ra = 8.374$ but this value varies with wavenumber. With decreasing wavenumber the turning point moves to lower values of Ra while with increasing wavenumber it moves to higher Rayleigh numbers.

The flow and temperature fields for the lower and the upper branch of the state shown in figure 6(*b*,*c*) reveal that the secondary solution R_1 consists of counter-rotating convection rolls. With increasing distance from the bifurcation point rolls grow in height while maintaining their width, so that their aspect ratio (height/width) increases. To quantify the growth in height we use the thickness $\delta_{\theta,99}$, defined as the distance to the plate at which the mean temperature profile reaches $0.01T_0$ for the first time. The definition of $\delta_{\theta,99}$ is illustrated in figure 7(*a*) using temperature profiles of both branches of R_1. The variation of the quantity $\delta_{\theta,99}$ with Ra for different Prandtl numbers for the lower and the upper branches of the roll solution is shown in figure 7(*b*). While for the lower branch of R_1 the height varies

https://doi.org/10.1017/jfm.2016.514 Published online by Cambridge University Press

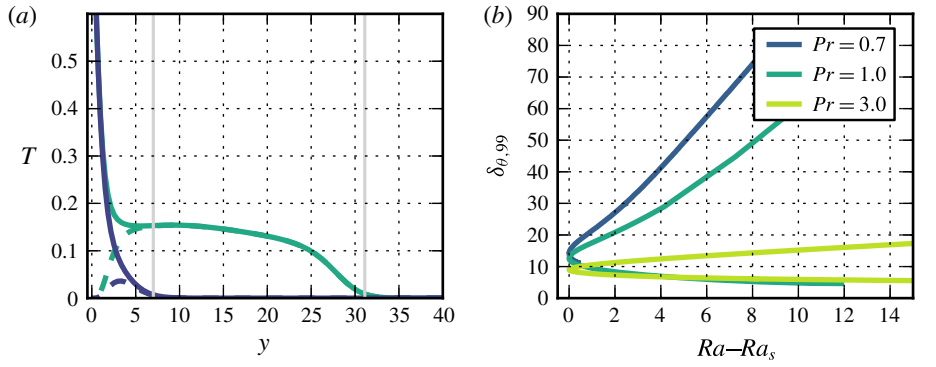


FIGURE 7. (Colour online) (*a*) Temperature profiles of the lower (blue) branch and upper branch (cyan) of the secondary solution R_1 at $Ra = 13$ versus distance y above the plate. For the total temperature profile a solid line is used and the deviations from the base profile are shown by dashed lines. The positions of $\delta_{\theta,99}$ are marked using grey lines. (*b*) Values of $\delta_{\theta,99}$ of the secondary solution R_1 in dependence on the distance to the saddle-node point for different Prandtl numbers. For each Prandtl number the wavelength of the state shown is chosen to be the critical wavelength at the particular value of the Prandtl number.

only slightly with Ra, the extension of the upper branch increases monotonically with the Rayleigh number. The rate of increase with Ra as well as the absolute values of the height depend strongly on the Prandtl number. For small values of Pr they are larger than for higher values of Pr. Specifically, the increase of the height of the upper branch solution with Rayleigh number follows a linear law (for sufficient distance from the turning point). The slope increases with decreasing Prandtl number from approximately 0.4 for $Pr = 3$ to 8.1 for $Pr = 0.7$. The results show that for small Prandtl number the roll solutions extend remarkably far above the plate, and their reach seems to increase with Ra, independent of Pr.

The secondary roll solutions have different heat transport properties than the base flow. In figure 8(*a*) the Nusselt number $\tilde{Nu}$ is shown as a function of Rayleigh number for the roll solution R_1 with $k = k_c$ and $Pr = 1$. To rationalize the negative values of $\tilde{Nu}$ the contributions of the convective and the conductive heat transport for a state on the upper branch of R_1 are shown as a function of y in figure 8(*b*). Especially for the upper branch, the heat transport due to convection has large negative values, leading to negative values of the integrated quantity $\tilde{Nu}$ with large modulus. The figure shows that for the secondary solution R_1 the conductive heat transport is only relevant close to the wall and quickly drops to zero for larger values of y. Furthermore, the plot illustrates that indeed the convective heat transport causes the large negative values of $\tilde{Nu}$ (the integral over the dashed curve). If only the deviations from the base flow are considered, the up-flow and down-flow regions in the roll state R_1 are approximately of equal strength (see figure 6*b*,*c*) and the temperatures in both regions are comparable as well. Since the base flow has a negative wall-normal component, the symmetry is broken and the negative contribution to the convective heat flux due to the down-flow region becomes larger than the positive contribution of the up-flow region. Thus, the average convective heat flux is negative for R_1. However, there are also turbulent states or coherent states with high asymmetry for which positive values of $\tilde{Nu}$ are obtained.

https://doi.org/10.1017/jfm.2016.514 Published online by Cambridge University Press

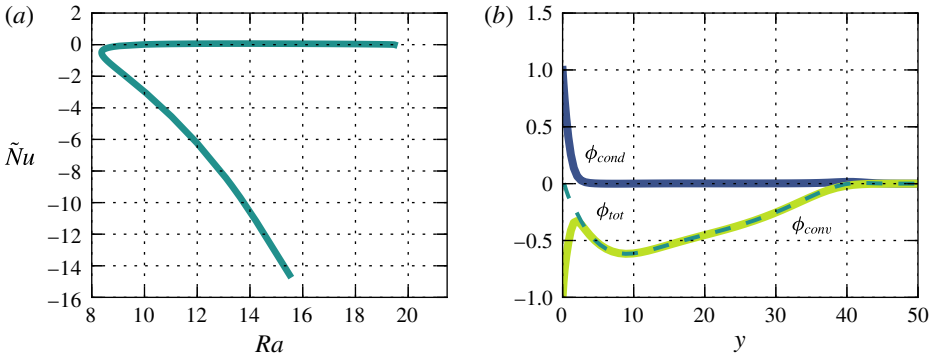


FIGURE 8. (Colour online) Nusselt number $\tilde{Nu}$ as a function of the Rayleigh number for the secondary solution R_1 with $k = k_c$ at $Re = 0$ is shown in (a). In (b) the contributions of the conductive (blue) and convective (yellow) heat flux are shown as functions of the wall-normal coordinate y for the upper branch of R_1 at $Ra = 15.5$. The resulting total heat flux is shown by the dashed cyan line. The quantities are normalized with respect to the Rayleigh number.

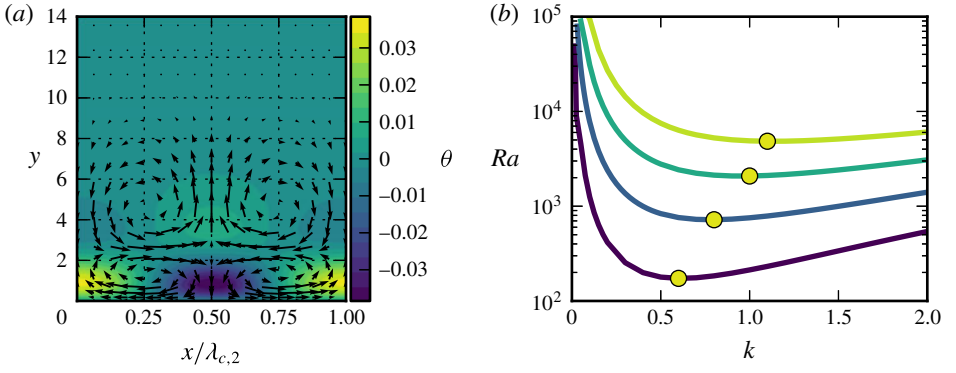


FIGURE 9. (Colour online) In (a) a visualization of the exact solution R_2 that bifurcates from the second two-dimensional instability is shown. The wavenumber is 0.612 and the Rayleigh number is 167. (b) Shows stability curves for the second to fifth two-dimensional unstable modes for $Pr = 1$. The critical Rayleigh numbers are marked with a yellow circle.

For high Rayleigh numbers another two-dimensional eigenmode becomes unstable. For $Pr = 1$, the critical wavenumber for this mode is 0.612 and the critical Rayleigh number is 173. This bifurcation is subcritical, and gives rise to an equilibrium solution henceforth referred to as R_2. The state R_2 has a set of four rolls staggered on top of each other, with the top pair similar to R_1 and the bottom one rather flat, as shown in figure 9(b). The second pair of rolls of the R_2 solution has its centre at a distance of approximately 5 from the plate where the temperature gradient is already quite low. This is reminiscent of the free-stream coherent structures of isothermal ASBL described by Deguchi & Hall (2014) and Kreilos *et al.* (2016), which have vortices at a distance to the plate where the shear gradient is low.

For even higher Rayleigh numbers further modes become unstable. Each additional unstable mode has one more layer of rolls. The stability curves for the second to fifth two-dimensional unstable modes are shown in figure 9(b). The critical Rayleigh numbers for the third, fourth and fifth unstable mode are 719.2, 2082 and 4846,

https://doi.org/10.1017/jfm.2016.514 Published online by Cambridge University Press

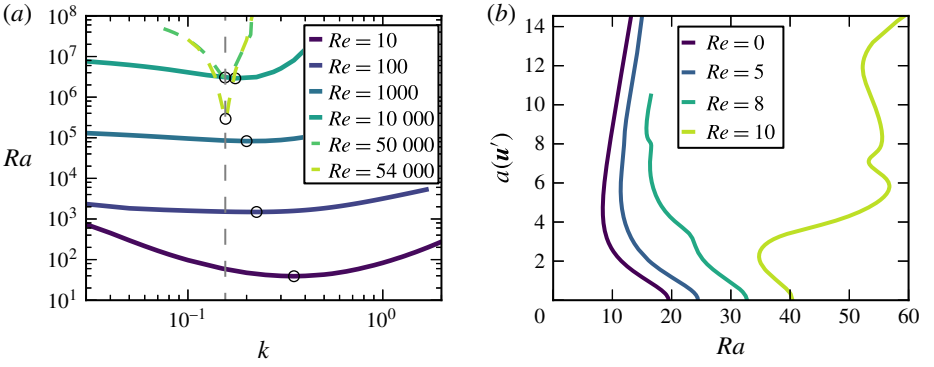


FIGURE 10. (Colour online) (*a*) Shows stability curves of the most unstable transversal mode in dependence on the Reynolds number. For each Reynolds number a black circle marks the critical Rayleigh number. The critical wavenumber of isothermal ASBL is marked by a dashed grey line. In (*b*) bifurcation diagrams of the two-dimensional transversal waves bifurcating from the laminar flow are shown for various Reynolds numbers.

respectively. The corresponding critical wavenumbers are 0.78, 1.0 and 1.1. Since they are very unstable, the ECS created in these bifurcation are of minor importance for the dynamics and thus not treated in this paper.

3.4. *Stability analysis for* $Re \neq 0$ *and* $Ra \neq 0$

The stability of the base flow for the case that shear and buoyancy are present can take advantage of the fact that a generalization of Squire's theorem holds for this flow (Gage & Reid 1968), so that it suffices to know the stability boundary for transversal and longitudinal modes to obtain a complete stability diagram.

A stability analysis of modes that depend only on the spanwise wavenumber and are invariant in the streamwise direction (longitudinal modes) yields, for any Prandtl number, the same critical Rayleigh numbers as in the case of vanishing Reynolds number.

Initially, for spanwise invariant modes (transversal modes) an increase of the Reynolds number has a stabilizing effect. Figure 10(*a*) shows stability curves of the most unstable transversal mode for various Reynolds numbers. Up to a Reynolds number of approximately 35 000 an increase of Re results in larger critical Rayleigh number. If the Reynolds number is further increased the transversal modes are rapidly destabilized again until at $Re_c = 54\,379$ they are unstable for $Ra = 0$. The critical wavenumbers move monotonically towards the critical wavenumber for the isothermal case with increasing Reynolds number.

We track the travelling wave solutions which bifurcate from the base flow when the transversal mode becomes unstable for various Reynolds numbers. The bifurcation diagrams of the transversal waves with $k = k_c = 0.4304$ in figure 10(*b*) show that for finite values of Re the bifurcation is still subcritical in the Rayleigh number, but the turning point of the solution branch moves to higher values of Ra.

For systems that are thermally stratified and under the influence of shear an often used dimensionless number is the Richardson number,

$$Ri = \frac{g\beta T_0 \delta}{U_\infty^2} = \frac{Ra}{Re^2 Pr}, \tag{3.11}$$

https://doi.org/10.1017/jfm.2016.514 Published online by Cambridge University Press

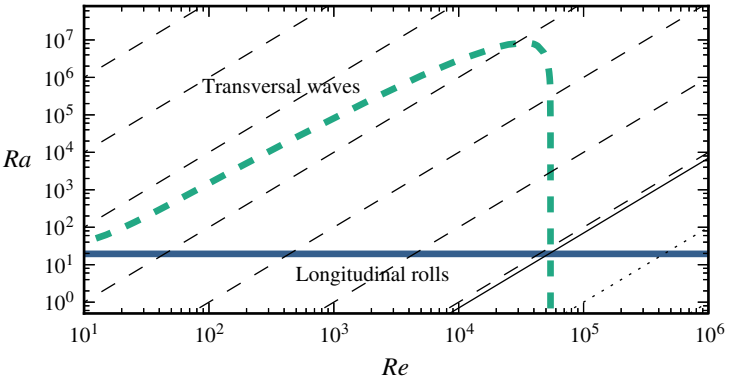


FIGURE 11. (Colour online) Stability diagram of TASBL in dependence on Ra and Re. Critical Rayleigh numbers for longitudinal rolls and transversal waves are shown using solid blue and dashed cyan lines. The solid black line corresponds to the critical Richardson number $Ri_c = 7 \times 10^{-9}$. where the instability switches from longitudinal rolls to transversal waves. Lines of constant Richardson number are shown using dashed and dotted lines for $Ri < Ri_c$ and $Ri > Ri_c$, respectively. The values of the Richardson numbers decrease by factors of 10^2 starting with 10^4 in the upper left corner.

which relates the buoyancy to the flow gradient. The value of Ri is a measure for the importance of natural convection compared to forced convection. As in the study of Gage & Reid (1968) for Rayleigh–Bénard–Poiseuille flow it is possible to give a critical value of the Richardson number which marks the transition between natural and forced convection. For ASBL over a heated plate we obtain a critical Richardson number of approximately $Ri_c = 19.47/(54379^2 \times 1.0) \approx 7 \times 10^{-9}$. For smaller Richardson numbers the system has an instability to transversal rolls or waves while for larger values of Ri the system has an instability to longitudinal rolls. The resulting complete stability diagram for the flow (for $Pr = 1$) with the critical Rayleigh numbers of transversal and longitudinal modes for different Re and lines of constant Richardson number, is shown in figure 11.

4. Two-dimensional solutions and subcritical transient chaos

In this section we analyse the stability of the two-dimensional secondary solutions and describe the bifurcating states. The analysis is restricted to the secondary states with a wavenumber equal to the critical one and to two-dimensional superharmonic disturbances with wavenumbers that are integer multiples of the ones of the secondary solution. The stability analysis of the solutions is performed using an Arnoldi method included in the Channelflow package and adapted to work with an additional temperature field. The calculations use a computational domain with $L_x = 0.1$, $L_z = \lambda_0$ and $L_y = 40$ and a resolution of $N_x \times N_y \times N_z = 4 \times 65 \times 32$, which is a good approximation of the two-dimensional system.

The stability analysis shows that the lower branch of the secondary solution R_1 has one unstable direction. Thus, it is an edge state (Skufca, Yorke & Eckhardt 2006; Schneider, Eckhardt & Yorke 2007) for the two-dimensional system because its stable manifold can separate two regions of the state space. Right after the turning point the upper branch of the solution is stable. When the Rayleigh number is increased, a pair of complex conjugate eigenvalues becomes unstable at $Ra \approx 9.15$, indicating a

https://doi.org/10.1017/jfm.2016.514 Published online by Cambridge University Press

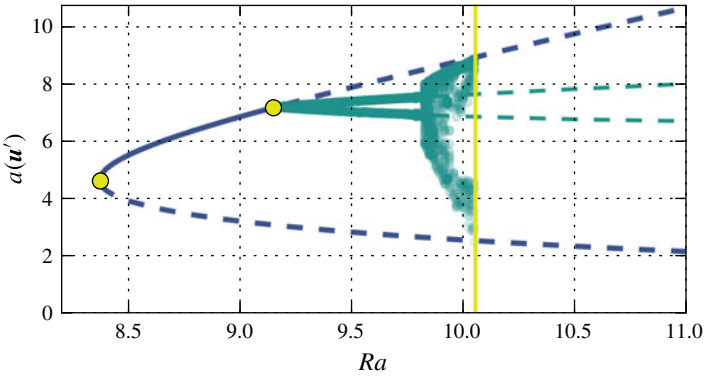


FIGURE 12. (Colour online) Bifurcation diagram of R_1 with wavenumber $k = k_c$ at $Pr = 1$ and $Re = 0$. The curve for R_1 is shown as a blue line. Chaotic and periodic states are indicated by cyan points representing minima and maxima of $a(\boldsymbol{u}')$ in the course of time. In addition the dashed cyan lines show the minimum and maximum of $a(\boldsymbol{u}')$ for the orbit PO_1. The bifurcation points of R_1 and PO_1 are marked by yellow circles. The solid yellow line marks the position of the boundary crisis bifurcation near $Ra = 10.0$ which destroys the attractor.

Hopf bifurcation. This bifurcation creates a stable periodic orbit which we refer to as PO_1 in the following. A supplementary movie illustrating the dynamics of the orbit is available online at http://dx.doi.org/10.1017/jfm.2016.514 (movie 1).

If the Rayleigh number is further increased, the periodic orbit undergoes a Neimark–Sacker bifurcation (Kuznetsov 1998) which creates a stable torus. Further bifurcations then create a chaotic attractor. A supplementary movie illustrating the dynamics of a trajectory on the chaotic attractor is available online (movie 2). The bifurcation diagram, sampled by plotting maxima of $a(\boldsymbol{u}')$ for trajectories on the attractor, is shown in figure 12. Eventually, the chaotic attractor is converted into a chaotic saddle by a boundary crisis bifurcation (e.g. Lai & Tél 2011). For $k = k_c$ this happens at $Ra \approx 10.06$. Following the boundary crisis, for $Ra < Ra_c$ initial conditions can be found which transiently show chaotic dynamics before they finally return to the base flow (supplementary movie 3 online). The bifurcation cascade that eventually creates transient chaos in this open flow is akin to those that were found to exist in internal flows such as plane Couette flow (Kreilos & Eckhardt 2012), pipe flow (Avila *et al.* 2013) or plane Poiseuille flow (Zammert & Eckhardt 2015). An important difference is that in the present case the exact solution which is the starting point of the cascade originates from a bifurcation of the base flow.

5. Three-dimensional states and localization

Up to this point we have considered two-dimensional exact coherent states, with a modulation in spanwise or streamwise and normal direction. Here, we turn to three-dimensional states, in particular states that are either extended or localized in both spanwise and streamwise direction. For all solutions in this section the Prandtl number is fixed at $Pr = 1$ and there is no flow, the Reynolds number is $Re = 0$.

5.1. *Straight rolls, squares and hexagons*

Using a Newton method we can identify different secondary solutions of the three-dimensional system which bifurcate from the base profile at the critical Rayleigh

https://doi.org/10.1017/jfm.2016.514 Published online by Cambridge University Press

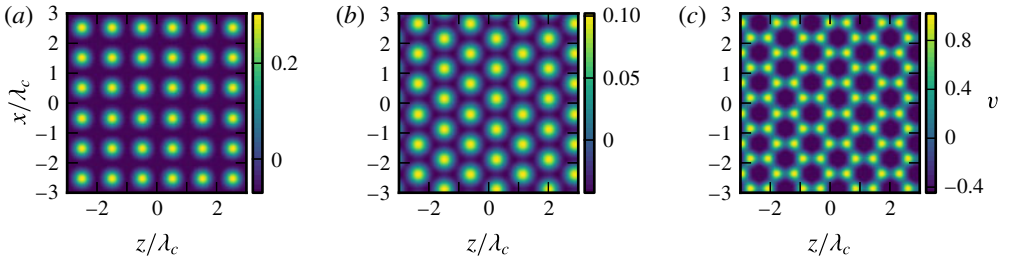


FIGURE 13. (Colour online) Visualization of the three-dimensional secondary solutions at $Ra = 17$. (*a*) Shows the square solution and (*b*,*c*) the hexagonal solutions of *l*- and *g*-type, respectively. For all panels the wall-normal velocity (deviation from laminar profile) is shown in a plane parallel to the plate at $y \approx 1.5$.

number. The simplest solutions which also exist in the two-dimensional case are straight rolls which are translationally invariant along an axis parallel to the plates. In addition to the straight rolls, a secondary solution exists which shows a square pattern of up-flow regions. This solution has equal wavenumbers in both directions parallel to the plate, as shown in figure 13(*a*). The visualization shows the wall-normal velocity in a plane parallel to the plate in a distance of 1.5. A continuation of this ECS in Rayleigh number shows that the turning point is at slightly lower Rayleigh numbers than for the two-dimensional roll solution R_1. The upper branch of this three-dimensional state again reaches remarkably far above the plates.

It is also possible to identify two different kinds of secondary solutions with hexagonal pattern. They are formed by superpositions of three solutions with wave vectors rotated by $2\pi/3$. One of the hexagonal patterns has a up-flow region in the centre of each hexagon while for the other one the centre contains the down-flow region. Following the nomenclature of Rayleigh–Bénard convection (Getling 1998) they can be named *l*- and *g*-cells. Visualization of both types of hexagons are shown in figure 13(*b*,*c*).

The bifurcation curves for a wavelength equal to the critical one of the square pattern are shown in figure 14. The figure shows that the bifurcation for the *g*-hexagons is initially supercritical and turns to lower *Ra* only with increasing amplitude, while *l*-hexagons bifurcate subcritically right from the base flow. The lowest values in *Ra* are achieved for *l*-hexagons.

For a given wavenumber the critical Rayleigh numbers for the square pattern and the hexagonal pattern differ slightly. The difference is too small to be noticeable in figure 14(*a*). In figure 14(*b*) the dependence of critical Rayleigh number on the wavenumber is shown for both patterns. In the presence of shear both the hexagonal and the square pattern instabilities move to higher Rayleigh numbers and the two-dimensional longitudinal rolls are the first instabilities to appear.

5.2. *Localized states*

With increasing distance to their bifurcation points the different secondary solutions undergo several three-dimensional instabilities. An interesting bifurcation of the square solution, which can be found in a domain with $L_x = L_z = 6\lambda_c$ and $L_y = 40$ (resolution $N_x \times N_y \times N_z = 192 \times 49 \times 192$), is located slightly below Ra_c. The bifurcation is connected with a long-wavelength instability (Chantry, Willis & Kerswell 2014; Melnikov, Kreilos & Eckhardt 2014) in two directions and creates a three-dimensional

https://doi.org/10.1017/jfm.2016.514 Published online by Cambridge University Press

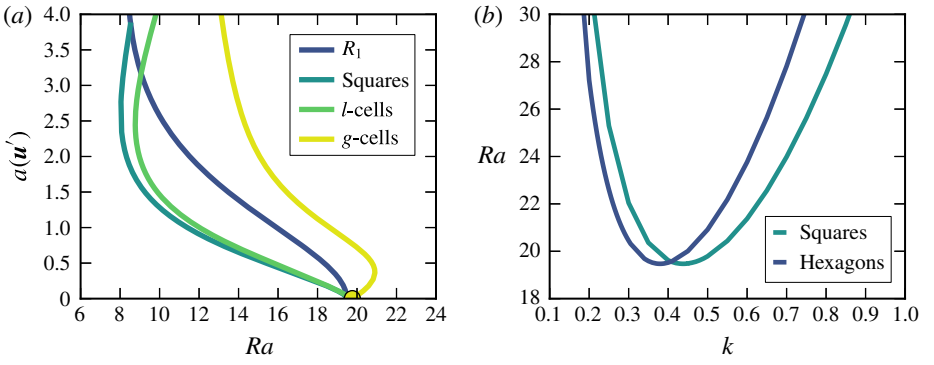


FIGURE 14. (Colour online) (*a*) Shows a bifurcation diagram of the four equilibrium patterns that exist in the three-dimensional system for $Re = 0$. For each solution the wavenumber is $k = k_c = 0.4305$. In (*b*) the stability lines for the hexagonal and the square instability are compared.

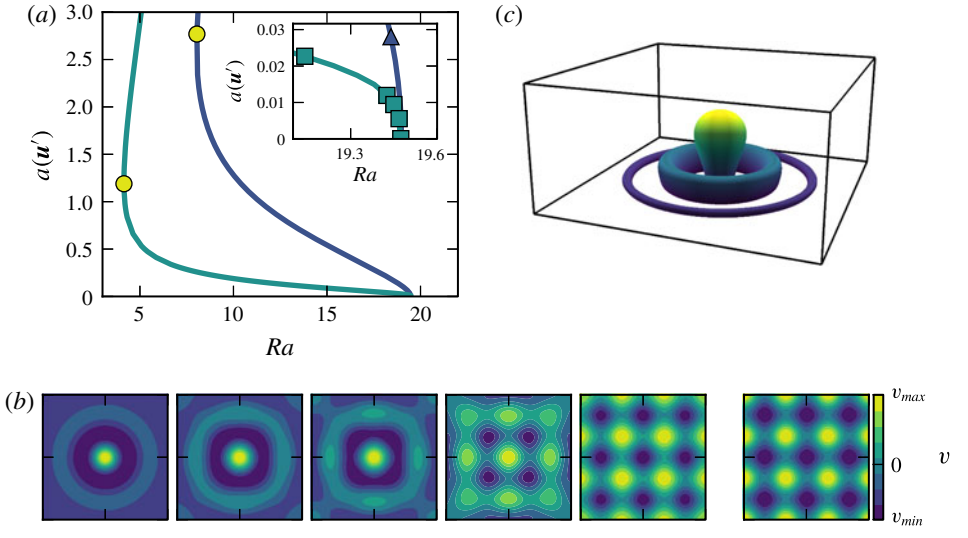


FIGURE 15. (Colour online) (*a*) Shows the bifurcation diagram for the doubly localized equilibrium solution C_1 (cyan) and the spatially extended equilibrium (blue). The inset shows the bifurcation diagram close to the point where C_1 connects to the spatially extended pattern. In (*b*) the states which are marked with the squares in the inset of (*a*) are visualized. The plots show the wall-normal velocity v in a plane parallel to the plate in a distance of 1.5. The leftmost picture corresponds to the square at the lowest Rayleigh number. The rightmost panel in (*b*) shows the wall-normal velocity v for the state marked in (*a*) by the triangle. In (*c*) the iso-surface $v = 0.0005$ (deviation from laminar) is shown for the doubly localized equilibrium C_1 at $Ra = 17.0$, $Re = 0$ and $Pr = 1$. The iso-surface is coloured according to the distance to the plate from blue to yellow.

solution which for lower Rayleigh numbers becomes spatially localized in both directions parallel to the plate. The bifurcation diagram in figure 15(*a*) shows the spatially extended square pattern together with the bifurcating solution. For the Rayleigh numbers marked in the bifurcation diagram flow visualizations of the

https://doi.org/10.1017/jfm.2016.514 Published online by Cambridge University Press

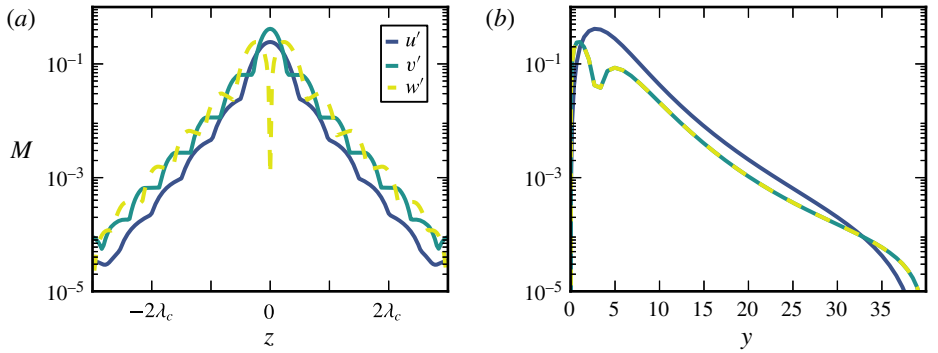


FIGURE 16. (Colour online) Maximal values M of the streamwise (blue), spanwise (yellow) and wall-normal (cyan) velocity component for the localized equilibrium at $Ra = 17$. (*a*) Shows the dependence on the wall-parallel coordinate z and (*b*) the dependence on the wall-normal coordinate y.

solutions are given in figure 15(*b*). The visualizations illustrate how the spatially extended pattern turns into localized states. Slightly below the bifurcation point, the flow pattern looks like the one of the spatially extended state with an additional modulation. With decreasing Rayleigh number this modulation quickly becomes larger until a localized and rotational symmetric state is reached.

The three-dimensional visualization of the state at $Ra = 17$ which is shown in figure 15(*c*) impressively illustrates the localization and the symmetry of the state. For localized convection states akin to the identified ECS but only localized in one spatial direction the term convecton has been introduced (e.g. Blanchflower 1999; Lo Jacono, Bergeon & Knobloch 2011; Beaume *et al.* 2013). Adopting this notation, we will call the doubly localized equilibrium a convecton and use the abbreviation C_1.

As a measure for the localization of the state C_1 we use the maximum norm,

$$M(u') = \max_{y,x} |u(x, y, z)'|, \tag{5.1}$$

here given for the streamwise component u and in dependence of the spanwise coordinate. In figure 16 the maximum norm of all velocity components in the wall-parallel (*a*) and wall-normal (*b*) directions are shown. Since the localization is quite strong, the state exists also in larger domains and is not an artefact of the boundary conditions. In the directions parallel to the plate and also in wall-normal direction, the decay of the velocities is in good agreement with an exponential decay. In contrast to the doubly localized exact solution found in plane Poiseuille flow (Zammert & Eckhardt 2014*b*), the decay does not become algebraic for large distances. The difference can be rationalized by the fact that in plane Poiseuille flow the shear creates a large-scale flow around the exact solution which decays algebraically. Since in the present case the Reynolds number is zero, there is no shear and no large-scale flow. Thus, the decay is exponential over a large range.

The turning point for C_1 lies at $Ra \approx 4.14$. Close to the turning point, the localization becomes weaker again and especially the upper branch becomes very wide and very difficult to track numerically.

In addition to the localized equilibrium C_1, many other localized states can be found. Starting with the spatially extended secondary solutions, we use two-dimensional

https://doi.org/10.1017/jfm.2016.514 Published online by Cambridge University Press

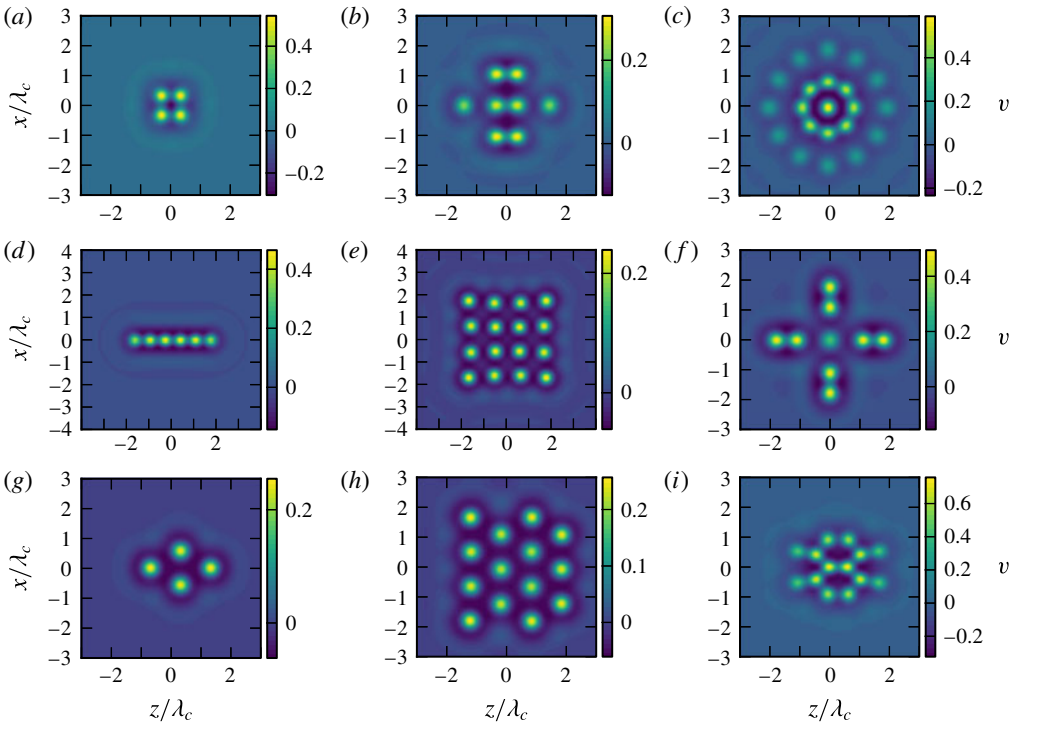


FIGURE 17. (Colour online) Different doubly localized solutions at $Ra = 17.8$. The Prandtl number is 1 and the Reynolds number is 0. The pictures show the wall-normal velocity in a plane parallel to the lower plate at $y \approx 1.5$.

window functions (Brand & Gibson 2014; Gibson & Brand 2014) to create initial guesses for Newton searches for localized equilibrium solutions. A two-dimensional window function $W(x, z)$ can be written as a product of two one-dimensional window functions. We use two different types of one-dimensional window functions, a Gaussian

$$W_1(x) = A \exp(-Bx^2) \tag{5.2}$$

and the function

$$W_2(x) = \frac{1}{4}\left(1 + \tanh\left(\frac{6(A-x)}{B} + 3\right)\right)\left(1 + \tanh\left(\frac{6(A+x)}{B} + 3\right)\right) \tag{5.3}$$

introduced by Gibson & Brand (2014). For appropriately chosen parameters A and B the obtained initial conditions are good initial guesses for equilibrium solutions. In figure 17 visualizations of different localized equilibrium solutions that were found for $Ra = 17.8$ and $Pr = 1$ are shown. The states shown in (*a–c*) were obtained from initial conditions created using the window function W_1 and for the state in (*d*,*e*) the window function W_2 was used. The equilibrium shown in (*f*) was obtained from an initial guess that was constructed by combining flow fields of several C_1 solutions. The states shown in (*g–i*) are obtained by applying window functions to the hexagonal patterns.

https://doi.org/10.1017/jfm.2016.514 Published online by Cambridge University Press

6. Summary and outlook

The present study extends the family of sheared convection problems from planar sheared convection (Clever & Busse 1992) and Poiseuille–Rayleigh–Bénard flow (Nicolas 2002) to the case of the ASBL, as a step towards analysing developing boundary layers. In all flows the transition is connected with roll states that are preferentially aligned with the flow direction, at least for Reynolds numbers close to the threshold. For higher Reynolds numbers, transverse rolls are preferred. The critical Rayleigh number shows a strong dependence on Prandtl number, which can be rationalized by relating it to an effective Rayleigh number that takes the temperature difference across the velocity field and the thickness of the thermal boundary layer into account.

The presence of a subcritical instability gives rise to a wide variety of secondary states, in particular of localized solutions of various shapes. While some of these states are reminiscent of plumes and other structures observed in thermal boundary layers, further studies of their dynamical properties will be required in order to establish this link more formally. It will be also be interesting to see how a spatial development as in Blasius boundary layers will influence the structures and their properties. Eventually, the study of the stability of convection combined with suitable boundary layer flows should provide a more reliable description of the transition from laminar to turbulent boundary layers and thus of the transition to the ultimate regime in thermal convection, (Grossmann & Lohse 2002).

Finally, it is intriguing that the upper branches of the coherent structures reach far into the free-stream region above the boundary layers. Certain ECS in shear boundary layers show similar properties (Deguchi & Hall 2014; Kreilos *et al.* 2016). The observation that the turbulent ASBL has remarkably thick boundary layers (Schlatter & Örlü 2011; Bobke, Örlü & Schlatter 2016) thus suggesting that a study of the thermally heated ASBL in conjunction with investigations of the various exact coherent structures could also shed light on the large scale properties and organization of the flow beyond the transitional regime discussed here.

Acknowledgements

We thank J. F. Gibson for providing and maintaining channelflow. This work was supported in parts by the Deutsche Forschungsgemeinschaft (DFG) within FOR 1182 and by Stichting voor Fundamenteel Onderzoek der Materie (FOM) within the program ‘Towards ultimate turbulence’.

Supplementary movies

Supplementary movies are available at http://dx.doi.org/10.1017/jfm.2016.514.

Appendix A. Direct numerical simulation

For the study of ASBL with heated plate the Channelflow code (Gibson 2012) was adapted to integrate the set of coupled equations (2.1)–(2.3). The velocity field is calculated as in the isothermal case, and the coupling of the temperature field on the velocity field is incorporated in the nonlinear part that is treated explicitly in the code.

The time integration of the temperature field is analogous to the velocity field. The total velocity field as well as the total temperature θ can be written as a sum of the

https://doi.org/10.1017/jfm.2016.514 Published online by Cambridge University Press

laminar or base profile and deviations,

$$\theta(\boldsymbol{x}) = \theta(\boldsymbol{x})' + T(y) \tag{A 1}$$

$$\boldsymbol{u}(\boldsymbol{x}) = \boldsymbol{u}(\boldsymbol{x})' + \boldsymbol{U}. \tag{A 2}$$

Equation (2.2) then gives

$$\partial_t \theta' + \underbrace{(\boldsymbol{u}\cdot\boldsymbol{\nabla})\theta}_{A(\boldsymbol{u},\theta)} = \underbrace{\kappa\,\Delta\theta'}_{D\theta} + \underbrace{\kappa\,\partial_y^2 T(y)}_{C}\,. \tag{A 3}$$

The time integration takes place in the Fourier-space, where the different terms in (2.2) become, symbolically,

$$\partial_t \tilde{\theta} + \tilde{A}(\boldsymbol{u},\theta) = \tilde{D}\tilde{\theta} + \tilde{C}. \tag{A 4}$$

Channelflow offers different time-integration schemes which were all adapted to work with the additional temperature field. Using the isothermal case described in the Channelflow manual as an example, we here explain the time stepping of the temperature field for the Crank–Nicolson/Adams–Bashforth scheme (CNAB2). Let $\tilde{\theta}^{n+1}$ denote the approximation to $\tilde{\theta}$ at time $n\Delta t$. Then, we first approximate the terms of (A 4) as follows:

$$\partial_t \tilde{\theta}^{n+1/2} = \frac{\tilde{\theta}^{n+1} - \tilde{\theta}^{n}}{2} + O(\Delta t) \tag{A 5}$$

$$\tilde{D}\tilde{\theta}^{n+1/2} = \tfrac{1}{2}\tilde{D}\tilde{\theta}^{n+1} + \tfrac{1}{2}\tilde{D}\tilde{\theta}^{n} + O(\Delta t) \tag{A 6}$$

$$\tilde{A}^{n+1/2} = \tfrac{3}{2}\tilde{A}^{n} - \tfrac{1}{2}\tilde{A}^{n-1} + O(\Delta t) \tag{A 7}$$

$$\tilde{C}\tilde{\theta}^{n+1/2} = \tfrac{1}{2}\tilde{C}^{n} + \tfrac{1}{2}\tilde{C}^{n-1} + O(\Delta t). \tag{A 8}$$

Substituting these approximations in (A 4) gives

$$\left[\frac{1}{\Delta t} - \frac{1}{2}\tilde{D}\right]\tilde{\theta}^{n+1} = \left[\frac{1}{\Delta t} + \frac{1}{2}\tilde{D}\right]\tilde{\theta}^{n} + \frac{3}{2}\tilde{A}^{n} - \frac{2}{2}\tilde{A}^{n-1}. \tag{A 9}$$

The right-hand side of this equation can be calculated directly since only previous time steps contribute to it. Equation (A 9) has the form of a Helmholtz equation,

$$\partial_y^2 \tilde{\theta}^{n+1} - \lambda\tilde{\theta}^{n+1} = R, \tag{A 10}$$

where

$$\lambda = \frac{1}{\Delta t} + 4\pi^2\nu\left(\frac{k_x^2}{L_x^2} + \frac{k_z^2}{L_z^2}\right) \tag{A 11}$$

$$R = \left[\frac{1}{\Delta t} + \frac{1}{2}D\right]\tilde{\theta}^{n} + \frac{3}{2}A^{n} - \frac{1}{2}A^{n-1} + \frac{1}{2}C^{n+1} + \frac{1}{2}C^{n}. \tag{A 12}$$

Routines for solving these equation are included in the Channelflow package since similar equations have to be solved for the velocity fields, too.

In addition to CNAB2 the other time steppers of Channelflow were adapted to handle an additional temperature field. In all cases, within one substep, the temperature is integrated forward first. For the calculation of $A(\boldsymbol{u},\theta)$ the velocity

https://doi.org/10.1017/jfm.2016.514 Published online by Cambridge University Press

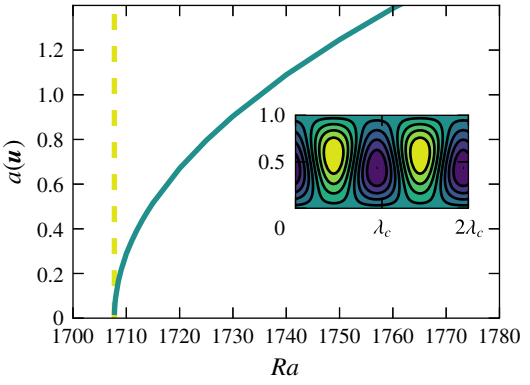


FIGURE 18. (Colour online) Bifurcation diagram of the Rayleigh–Bénard instability. The dashed yellow line marks the position for the theoretical critical Rayleigh number and the solid line shows the amplitude $a(\boldsymbol{u})$ of the convection solution. The inset shows the temperature field (deviation from conduction state) of the convection solutions at $Ra = 1880$.

field of the previous substep is used. Afterwards, the velocity field is integrated using a combination $(\theta^{n+1} + \theta^n)/2$ of the new and the old temperature fields. For the simulation of TASBL presented in this paper we use channeflow's SBDF3 integrator but double check some simulations using CNAB2.

To test our implementation several qualitative and quantitative test were performed. We calculated the critical Reynolds number of Rayleigh–Bénard-convection and compared our result to the known literature value $Ra = 1707.76$ (Busse 1978). A calculated bifurcation diagram for the critical wavenumber is shown in figure 18. The relative error in the critical Rayleigh number obtained with the code compared to the literature value was of order 10^{-5}. As a further (qualitative) test we considered sheared convection. Following the work of Clever & Busse (1992), the ECS in isothermal plane Couette flow was continued in Rayleigh number and shown to connect to the roll solution created by the thermal instability.

REFERENCES

AHLERS, G., GROSSMANN, S. & LOHSE, D. 2009 Heat transfer and large scale dynamics in turbulent Rayleigh–Bénard convection. *Rev. Mod. Phys.* **81** (2), 503–537.

AVILA, M., MELLIBOVSKY, F., ROLAND, N. & HOF, B. 2013 Streamwise-localized solutions at the onset of turbulence in pipe flow. *Phys. Rev. Lett.* **110**, 224502.

BEAUME, C., BERGEON, A., KAO, H.-C. & KNOBLOCH, E. 2013 Convectons in a rotating fluid layer. *J. Fluid Mech.* **717**, 417–448.

BLANCHFLOWER, S. 1999 Magnetohydrodynamic convectons. *Phys. Lett.* A **261**, 74–81.

BOBKE, A., ÖRLÜ, R. & SCHLATTER, P. 2016 Simulations of turbulent asymptotic suction boundary layers. *J. Turbul.* **17** (2), 157–180.

BRAND, E. & GIBSON, J. F. 2014 A doubly-localized equilibrium solution of plane Couette flow. *J. Fluid Mech.* **750**, R1.

BUSSE, F. H. 1978 Non-linear properties of thermal convection. *Rep. Prog. Phys.* **41**, 1929–1967.

CHANDRASEKHAR, S. 1961 *Hydrodynamic and Hydromagnetic Stability*. Clarendon Press.

CHANTRY, M., WILLIS, A. P. & KERSWELL, R. R. 2014 The genesis of streamwise-localized solutions from globally periodic travelling waves in pipe flow. *Phys. Rev. Lett.* **112**, 164501.

https://doi.org/10.1017/jfm.2016.514 Published online by Cambridge University Press

CHILLÀ, F. & SCHUMACHER, J. 2012 New perspectives in turbulent Rayleigh–Bénard convection. *Eur. Phys. J.* E **35**, 58.

CLEVER, R. M. & BUSSE, F. H. 1992 Three-dimensional convection in a horizontal fluid layer subjected to a constant shear. *J. Fluid Mech.* **234**, 511–527.

DEGUCHI, K. & HALL, P. 2014 Free-stream coherent structures in parallel boundary-layer flows. *J. Fluid Mech.* **752**, 602–625.

DIJKSTRA, H., WUBS, F. W., CLIFFE, A. K., DOEDEL, E., DRAGOMIRESCU, I. F., ECKHARDT, B., GELFGAT, A. Y., HAZEL, A. L., LUCARINI, V., SALINGER, A. G. *et al.* 2014 Numerical bifurcation methods and their applicaton to fluid dynamics: analysis beyond simulation. *Commun. Comput. Phys.* **15** (1), 1–45.

DU PUITS, R., LI, L., RESAGK, C., THESS, A. & WILLERT, C. 2013 Turbulent boundary layer in high Rayleigh number convection in air. *Phys. Rev. Lett.* **112**, 124301.

DUGUET, Y., PRINGLE, C. C. T. & KERSWELL, R. R. 2008 Relative periodic orbits in transitional pipe flow. *Phys. Fluids* **20** (11), 114102.

DUGUET, Y., SCHLATTER, P., HENNINGSON, D. S. & ECKHARDT, B. 2012 Self-sustained localized structures in a boundary-layer flow. *Phys. Rev. Lett.* **108**, 044501.

ECKHARDT, B., FAISST, H., SCHMIEGEL, A. & SCHNEIDER, T. M. 2008 Dynamical systems and the transition to turbulence in linearly stable shear flows. *Phil. Trans.* A **366**, 1297–1315.

ECKHARDT, B., SCHNEIDER, T. M., HOF, B. & WESTERWEEL, J. 2007 Turbulence transition in pipe flow. *Annu. Rev. Fluid Mech.* **39** (1), 447–468.

FAISST, H. & ECKHARDT, B. 2003 Traveling waves in pipe flow. *Phys. Rev. Lett.* **91**, 224502.

FRANSSON, J. H. M. & ALFREDSSON, P. H. 2003 On the disturbance growth in an asymptotic suction boundary layer. *J. Fluid Mech.* **482**, 51–90.

GAGE, K. S. & REID, W. H. 1968 The stability of thermally stratified plane Poiseuille flow. *J. Fluid Mech.* **33** (01), 21–32.

GETLING, A. V. 1998 *Rayleigh–Bénard Convection – Structures and Dynamics*. World Scientific.

GIBSON, J. F. 2012 Channelflow: a spectral Navier–Stokes simulator in C++. *Tech. Rep.*, University of New Hampshire.

GIBSON, J. F. & BRAND, E. 2014 Spanwise-localized solutions of planar shear flows. *J. Fluid Mech.* **745**, 25–61.

GIBSON, J. F., HALCROW, J. & CVITANOVIĆ, P. 2009 Equilibrium and travelling-wave solutions of plane Couette flow. *J. Fluid Mech.* **638**, 243–266.

GROSSMANN, S. 2000 The onset of shear flow turbulence. *Rev. Mod. Phys.* **72** (2), 603.

GROSSMANN, S. & LOHSE, D. 2000*a* Scaling in thermal convection: a unifying theory. *J. Fluid Mech.* **407**, 27–56.

GROSSMANN, S. & LOHSE, D. 2000*b* Thermal convection for large Prandtl numbers. *Phys. Rev. Lett.* **86**, 3316–3319.

GROSSMANN, S. & LOHSE, D. 2002 Prandtl and Rayleigh number dependence of the Reynolds number in turbulent thermal convection. *Phys. Rev.* E **66**, 016305.

HALCROW, J., GIBSON, J. F., CVITANOVIĆ, P. & VISWANATH, D. 2009 Heteroclinic connections in plane Couette flow. *J. Fluid Mech.* **621**, 365–376.

HOCKING, L. M. 1975 Non-linear instability of the asymptotic suction velocity profile. *Q. J. Mech. Appl. Maths* **28** (3), 341–353.

HOF, B., VAN DOORNE, C. W. H., WESTERWEEL, J., NIEUWSTADT, F. T. M., FAISST, H., ECKHARDT, B., WEDIN, H., KERSWELL, R. R. & WALEFFE, F. 2004 Experimental observation of nonlinear traveling waves in turbulent pipe flow. *Science* **305** (5690), 1594–1598.

KAWAHARA, G. & KIDA, S. 2001 Periodic motion embedded in plane Couette turbulence: regeneration cycle and burst. *J. Fluid Mech.* **449**, 291–300.

KHAPKO, T., DUGUET, Y., KREILOS, T., SCHLATTER, P., ECKHARDT, B. & HENNINGSON, D. S. 2014 Complexity of localised coherent structures in a boundary-layer flow. *Eur. Phys. J.* E **37**, 32.

KHAPKO, T., KREILOS, T., SCHLATTER, P., DUGUET, Y., ECKHARDT, B. & HENNINGSON, D. S. 2013 Localized edge states in the asymptotic suction boundary layer. *J. Fluid Mech.* **717**, R6.

https://doi.org/10.1017/jfm.2016.514 Published online by Cambridge University Press

KHAPKO, T., SCHLATTER, P., DUGUET, Y. & HENNINGSON, D. S. 2016 Turbulence collapse in a suction boundary layer. *J. Fluid Mech.* **795**, 356–379.

KREILOS, T. & ECKHARDT, B. 2012 Periodic orbits near onset of chaos in plane Couette flow. *Chaos* **22** (4), 047505.

KREILOS, T., GIBSON, J. F. & SCHNEIDER, T. M. 2016 Localized travelling waves in the asymptotic suction boundary layer. *J. Fluid Mech.* **795**, R3.

KREILOS, T., VEBLE, G., SCHNEIDER, T. M. & ECKHARDT, B. 2013 Edge states for the turbulence transition in the asymptotic suction boundary layer. *J. Fluid Mech.* **726**, 100–122.

KUZNETSOV, Y. A. 1998 *Elements of Applied Bifurcation Theory*. Springer.

LAI, Y.-C. & TÉL, T. 2011 *Transient Chaos – Complex Dynamics on Finite Time Scales*. Springer.

LANDAU, L. D. & LIFSCHITZ, E. M. 1959 *Fluid Mechanics*. Pergamon Press.

LO JACONO, D., BERGEON, A. & KNOBLOCH, E. 2011 Magnetohydrodynamic convectons. *J. Fluid Mech.* **687**, 595–605.

MARATI, N., DAVOUDI, J., CASCIOLA, C. M. & ECKHARDT, B. 2006 Mean profiles for a passive scalar in wall-bounded flows from symmetry analysis. *J. Turbul.* **7**, N61.

MELNIKOV, K., KREILOS, T. & ECKHARDT, B. 2014 Long-wavelength instability of coherent structures in plane Couette flow. *Phys. Rev.* E **89**, 043008.

MERKIN, J. H. 1972 Free convection with blowing and suction. *Intl J. Heat Mass Transfer* **15** (5), 989–999.

MILINAZZO, F. A. & SAFFMAN, P. G. 1985 Finite-amplitude steady waves in plane viscous shear flows. *J. Fluid Mech.* **160**, 281–295.

MOFFAT, J. & KAYS, W. M. 1968 The turbulent boundary layer on a porous plate: experimental heat transfer with uniform blowing and suction. *Intl J. Heat Mass Transfer* **11**, 1547–1566.

NAGATA, M. 1990 Three-dimensional finite-amplitude solutions in plane Couette flow: bifurcation from infinity. *J. Fluid Mech.* **217**, 519–527.

NAGATA, M. & DEGUCHI, K. 2013 Mirror-symmetric exact coherent states in plane Poiseuille flow. *J. Fluid Mech.* **735**, R4.

NICOLAS, X. 2002 Bibliographical review on the Poiseuille–Rayleigh–Bénard flows: the mixed convection flows in horizontal rectangular ducts heated from below. *Intl J. Therm. Sci.* **41**, 961–1016.

PARODI, A., VON HARDENBERG, J., PASSONI, G., PROVENZALE, A. & SPIEGEL, E. 2004 Clustering of plumes in turbulent convection. *Phys. Rev. Lett.* **92**, 194503.

PRINGLE, C. C. T. & KERSWELL, R. R. 2007 Asymmetric, helical, and mirror-symmetric traveling waves in pipe flow. *Phys. Rev. Lett.* **99**, 074502.

SCHLATTER, P. & ÖRLÜ, R. 2011 Turbulent asymptotic suction boundary layers studied by simulation. *J. Phys.: Conf. Ser.* **318** (2), 022020.

SCHLICHTING, H. & GERSTEN, K. 1997 *Grenzschicht-Theorie*. Springer.

SCHMID, P. & HENNINGSON, D. S. 2001 *Stability and Transition in Shear Flow*. Springer.

SCHMIEGEL, A. 1999 Transition to turbulence in linearly stable shear flows. PhD thesis, Philipps-Universitität Marburg, http://archiv.ub.uni-marburg.de/diss/z2000/0062/.

SCHNEIDER, T. M., ECKHARDT, B. & YORKE, J. 2007 Turbulence transition and the edge of chaos in pipe flow. *Phys. Rev. Lett.* **99**, 034502.

SKUFCA, J., YORKE, J. A. & ECKHARDT, B. 2006 Edge of chaos in a parallel shear flow. *Phys. Rev. Lett.* **96**, 174101.

SPARROW, E. M. & CESS, R. D. 1961 Free convection with blowing and suction. *Trans. ASME J. Heat Transfer* **83** (3), 387–389.

TREFETHEN, L. N. 2000 *Spectral Methods in MATLAB*. Society for Industrial and Applied Mathematics.

VISWANATH, D. 2007 Recurrent motions within plane Couette turbulence. *J. Fluid Mech.* **580**, 339–358.

WALEFFE, F. 2001 Exact coherent structures in channel flow. *J. Fluid Mech.* **435**, 93–102.

WEDIN, H., CHERUBINI, S. & BOTTARO, A. 2015 Effect of plate permeability on nonlinear stability of the asymptotic suction boundary layer. *Phys. Rev.* E **92**, 013022.

https://doi.org/10.1017/jfm.2016.514 Published online by Cambridge University Press

WEDIN, H. & KERSWELL, R. R. 2004 Exact coherent structures in pipe flow: travelling wave solutions. *J. Fluid Mech.* **508**, 333–371.

ZAMMERT, S. & ECKHARDT, B. 2014*a* Periodically bursting edge states in plane Poiseuille flow. *Fluid Dyn. Res.* **46**, 041419.

ZAMMERT, S. & ECKHARDT, B. 2014*b* Streamwise and doubly-localised periodic orbits in plane Poiseuille flow. *J. Fluid Mech.* **761**, 348–359.

ZAMMERT, S. & ECKHARDT, B. 2015 Crisis bifurcations in plane Poiseuille flow. *Phys. Rev.* E **91**, 041003(R).

ZHOU, Q., SUN, C. & XIA, K.-Q. 2007 Morphological evolution of thermal plumes in turbulent Rayleigh–Bénard convection. *Phys. Rev. Lett.* **98**, 074501.

ZHOU, Q. & XIA, K. Q. 2010 Physical and geometrical properties of thermal plumes in turbulent Rayleigh–Bénard convection. *New J. Phys.* **12**, 075006.

ZOCCHI, G., MOSES, E. & LIBCHABER, A. 1990 Coherent structures in turbulent convection, an experimental study. *Phys.* A **166** (3), 387–407.

https://doi.org/10.1017/jfm.2016.514 Published online by Cambridge University Press